Fine details of sixfold Dirac fermions in pyrite-structured $PdSb_2$

Woori Ju,* Jinwon Jeong,* En-Jin Cho, and Han-Jin Noh†
Department of Physics, Chonnam National University, Gwangju 61186, Korea

Kyoo Kim‡
Korea Atomic Energy Research Institute, Daejeon 34057, Korea

Byeong-Gyu Park
Pohang Accelerator Laboratory, Pohang University of Science and Technology, Pohang 37673, Korea

(Received 8 March 2022; accepted 1 November 2022; published 15 November 2022)

We report detailed angle-resolved photoemission measurements on the electronic structure of an unconventional multifold Dirac fermionic semimetal $PdSb_2$ with a pyrite structure. By exploiting the photon energy and polarization dependence of the matrix element in photoemission intensity and by comparing photoemission data with *ab initio* band calculations, we experimentally identify the exact electronic structure, including the orbital characters of the electron pockets at the R point in the Brillouin zone of $PdSb_2$. Each electron pocket and hole-pocket-like structure consists of three doubly degenerate parabolic bands, respectively, which cross one another at the R point, forming a sixfold Dirac fermion. The overall electronic structure is consistent with the band calculations, but the gap size between two sextuple points is very sensitive to the Wyckoff position of Sb atoms, which is a result of the competition between the band energies and crystal symmetries.

DOI: 10.1103/PhysRevB.106.205125

I. INTRODUCTION

Topological properties in the electronic structure of a solid system has been one of the most important subjects in contemporary condensed matter physics [1–3]. At the early stage of the research, attention was paid to the question of what the essential ingredients are for topological nontriviality in crystalline systems. Large spin-orbit coupling in valence or conduction bands was pointed out to be essential to make a band inversion, which induces a topological phase transition, making robust topological metallic surface states phenomenological evidence in the electronic structure [4–6]. Another type of topological state was also realized to be possible if we can stably control the strength of a band-inversion parameter like spin-orbit coupling [7–9]. At a critical value of the control parameter, a topological phase transition occurs in touching a valence band maximum to a conduction band minimum point. The more intriguing thing is that the critical point can be stabilized not only by the control parameter but also by the symmetries of a crystal structure [10]. This so-called Dirac point (DP) is quite unique in several aspects, one of which is linear dispersion of bands around a DP. The linear energy-momentum dispersion relation enables us to introduce a relativistic quasiparticle (QP) concept using the similarity to the solution of a Dirac equation for a free massless particle [11]. Furthermore, it can be applied to an inversion-asymmetric or time-reversal asymmetric system, named a Weyl fermion [12]. The Weyl fermionic systems are more intriguing because no counterpart particle has been discovered yet in particle physics and it can be regarded as a magnetic monopole in energy-momentum space.

The QP concept is useful for classification of topological materials. In contrast to real particles that satisfy the Lorentz invariance, QPs do not have such constraints, which allows an extension to so-called type-II Dirac/Weyl (DW) fermions [13–15]. There is also another type of extension in relativistic QPs. While the conventional DW fermions correspond to spin-half particles, there can be multiband crossing DW points that are stabilized by crystal symmetries in some kinds of crystals. These points can be regarded as multifold DW fermions which correspond to particles with a larger spin number than half. The types of QPs in this category are eventually constrained by the symmetry set of host crystals, which must be one of the 230 space groups. Thus, group analysis can provide a full list of possible multifold fermion types in crystalline solid systems as in Ref. [16]. Threefold, sixfold, or eightfold DW fermions are stabilized in a system that belongs to one of 16 space groups.

Experimental confirmations by angle-resolved photoemission spectroscopy (ARPES) have been performed on several prototypical systems such as MoP, CoSi, and AlPt, where threefold DW fermions, threefold and fourfold chiral fermions, and fourfold and sixfold chiral fermions were observed [17–19]. While these systems have QPs with nonzero large Chern numbers, experimental confirmation on multifold fermionic systems with zero Chern number are rather rare.

*These authors contributed equally to this work.
†ffnhj@jnu.ac.kr
‡To whom correspondence on band calculations should be addressed: qkyooq@gmail.com

Only a few studies on $PdSb_2$ have been reported [20–22]. Even though previous studies by ARPES have shown that pyrite-structured $PdSb_2$ hosts sixfold degenerate fermionic QPs, a detailed study on the three-dimensional bulk electronic structure and orbital characters of the sixfold Dirac fermions near the R point in the Brillouin zone (BZ) of $PdSb_2$ is still lacking. It could help us to understand the origin of the topological phase of the system. For this purpose, we report here a detailed angle-resolved photoemission study on the three-dimensional electronic structure of an unconventional multifold Dirac fermionic semimetal $PdSb_2$ with a pyrite structure. In this paper, we exploit the photon energy and the photon polarization dependence of the matrix element in a photoemission process to reveal the exact electronic structure, including the orbital characters of the electron pockets at R in the BZ. Each electron pocket and hole-pocket-like structure consists of three doubly degenerate parabolic bands, respectively, which cross one another at the R point, forming a sixfold Dirac fermion. The overall electronic structure is consistent with *ab initio* band calculation results, but the gap size between two sextuple points is very sensitive to the Wyckoff position of Sb atoms, which reflects the competition between the band energies and the crystal symmetries.

II. EXPERIMENTAL METHODS

Pyrite-structured $PdSb_2$ single crystals were grown by the self-flux method, as can be found in literature [23]. A mixture of Pd (99.95%) and Sb (99.9%) powders with a 1:2.2 ratio was loaded in an evacuated quartz ampoule. The ampoule was heated to 1000 °C for 24 hours, followed by slow cooling to 700 °C at a rate of 3 °C/h, successive cooling to 500 °C at a rate of 10 °C/h, then furnace cooled to room temperature. Single crystals with a size of $\sim 3 \times 3 \times 2$ mm^3 were obtained. The single phase of the crystals and the pyrite-type structure were checked by x-ray diffraction.

ARPES measurements were performed at the 4A1 beamline of the Pohang Light Source with a Scienta R4000 electron spectrometer and $\hbar\omega = 35 \sim 110$ eV photons [24]. The crystals were cleaved *in situ* by a top-post method at 60 K under $\sim 7.0 \times 10^{-11}$ Torr. The cleavage always has a (001) normal direction, which was checked by low-energy electron diffraction. The total energy (momentum) resolution of ARPES data is ~25 meV (~0.01 Å^{-1}). For k_z mapping, we used a so-called inner potential method, in which the normal component of the electron momentum to the cleaved surface is given by the relation $k_z = \hbar^{-1}\sqrt{2m(E_{\rm kin}\cos^2\theta + V_0)}$. Here, m, $E_{\rm kin}$, θ, and V_0 are the electron mass, the kinetic energy of photoelectrons, the emission angle from the sample normal, and the inner potential, respectively [25]. For $PdSb_2$, the inner potential of 28.0 eV was taken in literature [21]. For the polarization-dependent ARPES measurements, the experimental geometry was fixed and the photon polarization was changed using the polarizing undulators in the beamline.

For the bulk band structure calculations, we have used the full potential local orbital code (FPLO). The relativistic effects are treated within full four-component Kohn-Sham-Dirac theory [26]. We adopted $12 \times 12 \times 12$ **k** points mesh in the full BZ for the reciprocal space integration. For the structure relaxation using the Feynmann-Hellman force, we have used OPENMX code [27]. To analyze the surface bands, we obtained the Wannier function tight-binding Hamiltonian from the bulk band structure and constructed a 20-layer slab Hamiltonian from the bulk Hamiltonian. We also obtained surface band structures using the Green's function method implemented in the FPLO code.

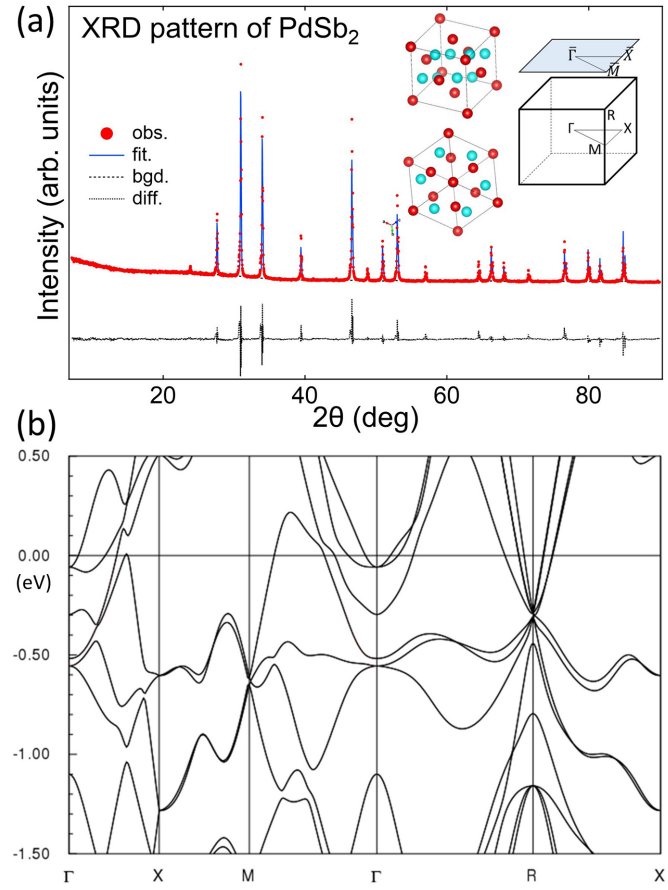

FIG. 1. Crystal structure and calculated band structure of $PdSb_2$. (a) X-ray powder diffraction pattern of pyrite-structured $PdSb_2$. Inset: Top left: Bird's-eye view of a pyrite structure. Bottom left: (111) view that shows threefold rotoinversion symmetry. Right: (001) surface- and bulk-Brillouin zone of a pyrite structure. (b) A calculated bulk band structure by the GGA method.

III. RESULTS AND DISCUSSION

Pyrite-structured $PdSb_2$ belongs to space group $Pa\bar{3}$ (No. 205), the symbol of which means that the system has a-axis glide symmetry and threefold rotoinversion symmetry in a primitive unit cell. The combination of the crystal symmetry operations and time-reversal symmetry was theoretically shown to make sixfold degeneracy at a time-reversal invariant momentum point R in the BZ [16]. Figure 1(a) shows the powder XRD pattern with a Rietveld fitting result and a constructed crystal structure from the pattern analysis in the top-left part of the inset [28]. The (111) view of the structure in the bottom-left part of the inset reveals the threefold rotoinversion symmetry. The obtained lattice constant a is 6.4585(1) Å and the Sb atom position parameter x for the Wyckoff position 8c is 0.3745 [29]. These are very consistent

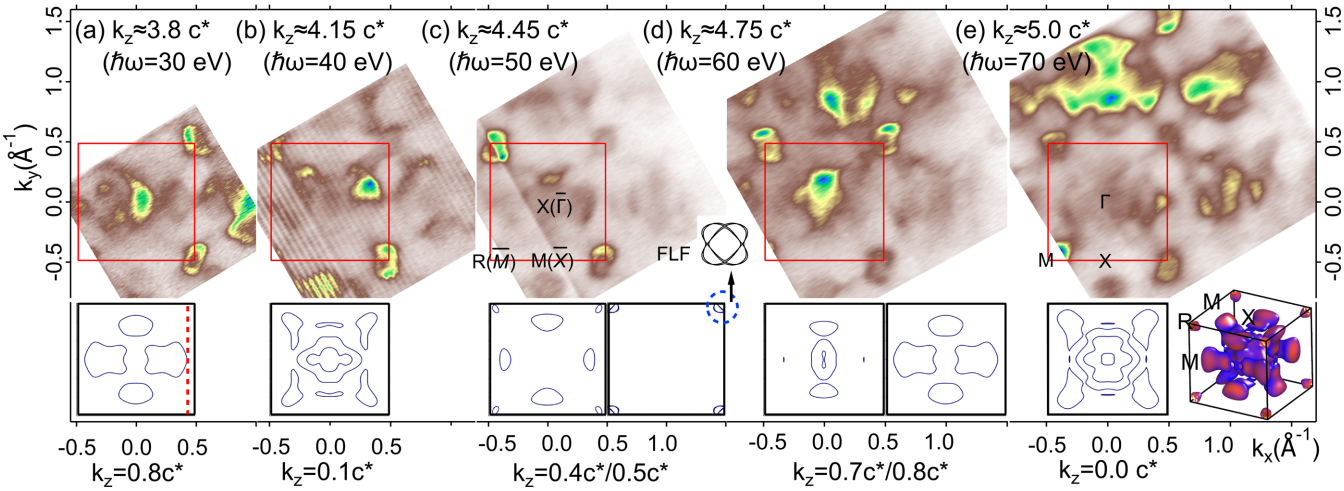

FIG. 2. ARPES-measured Fermi surfaces of $PdSb_2$. Each FS was obtained with photon energy (a) 30 eV, (b) 40 eV, (c) 50 eV, (d) 60 eV, and (e) 70 eV, respectively. The corresponding crystal momentum along the surface normal direction, k_z, is approximately (a) 3.8c*, (b) 4.15c*, (c) 4.45c*, (d) 4.75c*, and (e) 5.0c*, respectively. The calculated FSs in each panel are for comparison.

with the values in literature [30]. The BZ with major high symmetric points is shown in the right part of the inset, and a calculated bulk band structure of $PdSb_2$ along the high symmetric lines is displayed in Fig. 1(b). Since four Pd atoms and eight Sb atoms form a unit cell, the band structure consists of 20 Pd 4*d* orbitals and 24 Sb 5*p* orbitals. The bands were confirmed to have well-mixed *p*-*d* orbital characters and fully mixed atomic contribution. The overall structure looks similar to the previously reported calculation results [20,21], but a detailed comparison to the ARPES measurements in this paper reveals the necessity of a fine tuning in the band calculation as we describe below.

Figures 2(a)–2(e) show our ARPES-measured Fermi surfaces (FSs) with various photon energies. The field of view in a momentum space increases with the increase of photon energy in ARPES, so a larger area of FS is measured with a higher photon energy. The surface normal component of the electron momentum, k_z, in each panel was determined using the inner potential method, but its validity should be carefully taken into account due to the intrinsic two-dimension (2D)-friendly property as it appears in these data [25]. To be more specific in our case, the structures near the Γ point in the ARPES-measured FSs of Fig. 2(e) show similar features in part to those of calculations in the bottom panel but they also show a few extra structures that are not seen in the calculation images. They look more apparent in the other nonzero k_z value panels. Extra structures like those are often observed by ARPES in three-dimensional systems [15], and the possible mechanisms are well documented in literature [31]. If they are not due to an extrinsic effect, they are either surface states or $k_\perp$-projected bulk states. Comparing ARPES images to calculations indicates that the extra structures around Γ (or $\bar{\Gamma}$) are mainly the $k_\perp$-projected contributions.

In contrast to the structures near Γ, the structure near *R* or $\bar{\text{M}}$ appears in all the ARPES-measured maps. If the resolving power for $k_\perp$ is good enough in ARPES, the structure would be seen only in Fig. 2(c). We attribute it also to a considerable amount of surface-state contributions, which was checked in our surface-band calculations [32]. One noticeable thing is the shape of the structure. Considering the symmetries with respect to *R*, i.e., two mirror plane symmetries orthogonal to each other, it should look like a four-leaf flower (FLF hereinafter) as in Fig. 2(c). However, its appearance changes with position and photon energy, indicating the matrix element effect in photoemission process. The feature will be exploited to analyze the sixfold degeneracy of the DP in FLF.

In Figs. 3(a)–3(d), we display ARPES-measured dispersion relations along four major high-symmetric lines with the calculated bulk energy bands. As is the previous case in Fig. 2, the ARPES images also contain many more bands than the theoretical bulk bands. The extra bands are trackable if we take into account the 2D-friendly property of ARPES. The most apparent extra structure is band a_1 in Fig. 3(a). A very similar structure denoted as b_1 is observed in Fig. 3(b). The origin of these states is inferred to a $k_\perp$-projection effect in ARPES if we notice that the *M*-*X*-*M* line and the Γ-*X*-Γ line in Fig. 2(e) are orthogonal at $\bar{\text{X}}$ in a (001) surface BZ. Bands a_1 and b_1 are the identical structures measured in a different direction. The true measured position of band a_1 is 0.05c* off the $\bar{\text{M}}$-$\bar{\text{X}}$ line with k_z=0.35c* in our calculations [see the red dotted line in the bottom of Fig. 2(a)]. Electron pockets a_2 and d_1 also can be explained in a similar way. Points *M* and *R* are identical to $\bar{\text{M}}$ in a (001) surface BZ, and the same is true of Γ and *X*. The calculated bulk electron pockets at Γ in Fig. 3(c) are also perfectly captured in Fig. 3(d). Thus, the measured bulk energy bands and the calculated ones show good agreement with each other if we appropriately take into account the $k_\perp$-projection effect in ARPES.

Figure 4 shows a detailed structure analysis of the FLF at the *R* point based on our ARPES measurements and band calculations. Since the unit cell of a pyrite structure has four distinct Pd sites, the FLF consists of four spin-degenerate Pd 4*d* orbitals, each of which is contributed from the palladium atom at each site. In Figs. 4(a) and 4(b), the four calculated bands denoted as F_1–F_4 for each case of x=0.35 and 0.38 (Wyckoff position parameter 8*c* in a pyrite structure) are displayed along the *M*-*R*-*X* direction, respectively. In the

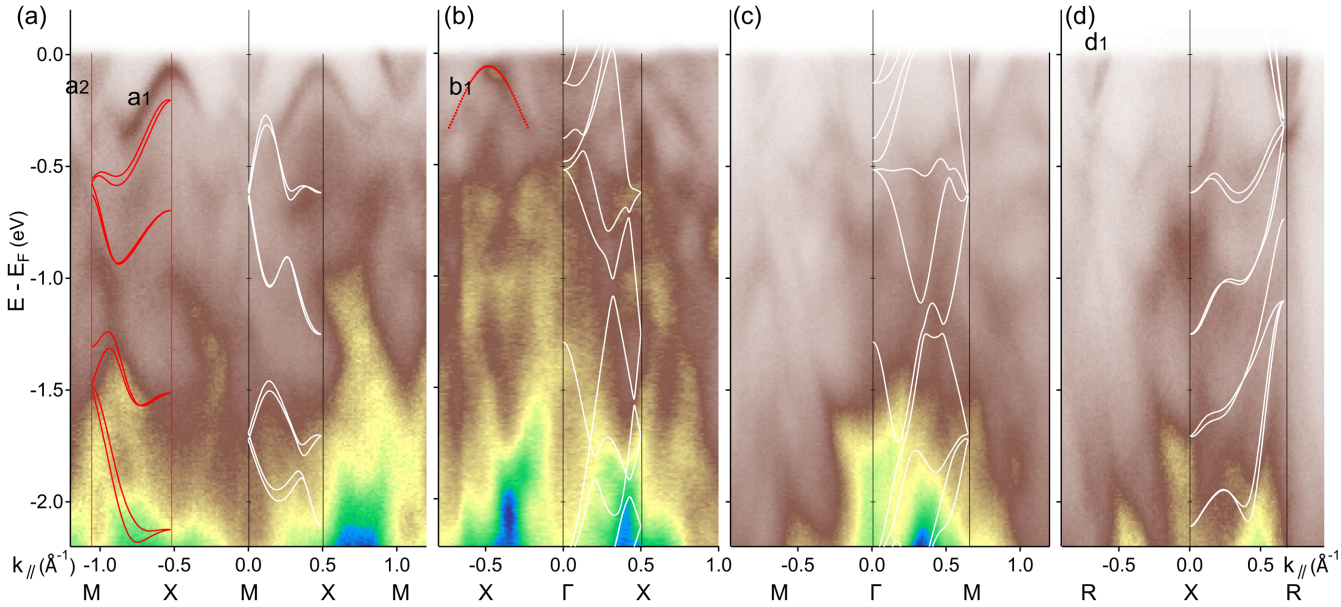

FIG. 3. ARPES-measured electronic band structure of $PdSb_2$. ARPES-measured dispersion relations along the high symmetric line of (a) *X*-*M*-*X*, (b) *X*-Γ-*X*, (c) *M*-Γ-*M*, and (d) *R*-*X*-*R*. The white lines in the ARPES data are the calculated bulk energy bands. The red lines in (a) are the calculated bulk energy bands along $\bar{M}$-$\bar{X}$ with k_z=0.35c*. The red curve denoted as b_1 in (b) is a guide to the eye.

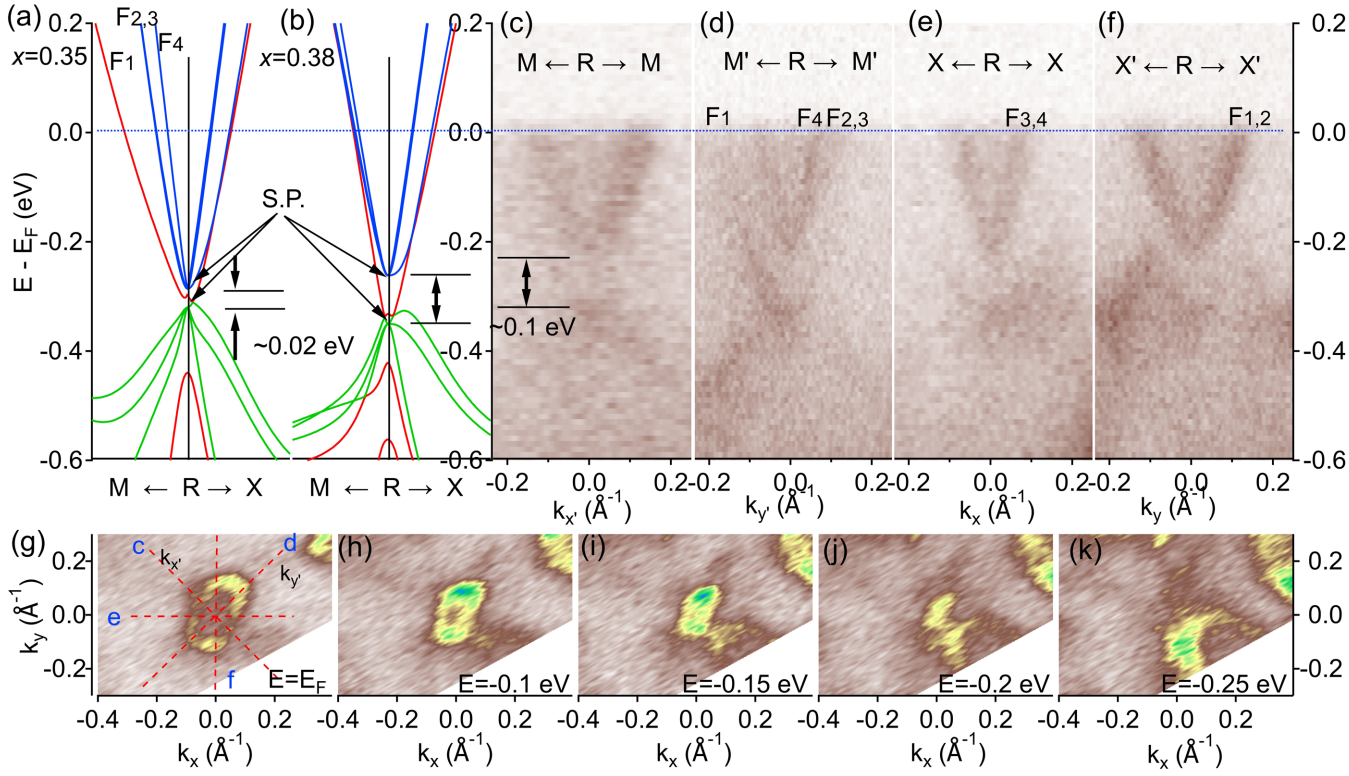

FIG. 4. Detailed structure of the FLF at *R*. Calculated band structure of the FLF along *M*-*R*-*X* line with Sb atomic position parameter (a) $x = 0.35$ and (b) $x = 0.38$. The blue and green lines form a sixfold degenerate Dirac point, or sextuple point (S.P.), respectively. ARPES-measured band structure of the FLF along (c) *M*-*R*-*M*, (d) *X*-*R*-*X*, (e) *M'*-*R*-*M'*, and (f) *X'*-*R*-*X'*. ARPES intensity map at a constant energy of (g) E_F, (h) $E = -0.1$ eV, (i) -0.15 eV, (j) -0.2 eV, and (k) -0.25 eV. Each red dotted line denoted with **c**–**f** in (g) corresponds to panels (c)–(f), respectively.

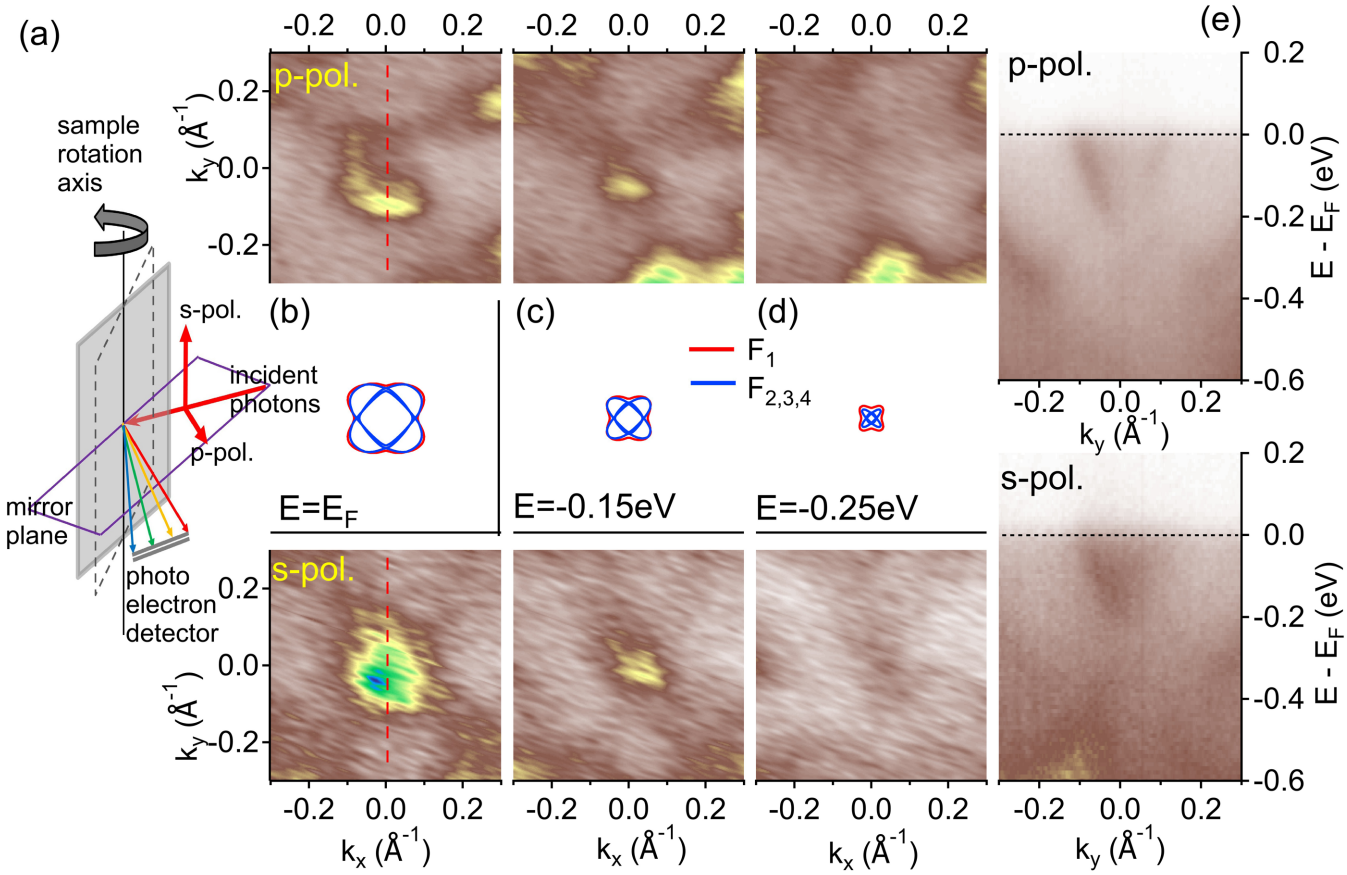

FIG. 5. Polarization-dependent ARPES data of $PdSb_2$. (a) Schematic diagram of the experimental setup. Upper (lower) panel shows a constant energy map measured in the $p(s)$-polarization mode at the energy of (b) E_F, (c) −0.15 eV, and (d) −0.25 eV. Each middle panel shows the calculated map of the FLF at the corresponding energy. (e) ARPES-measured dispersion image measured along the direction of the red dotted line in (b). Upper (lower) data is for $p(s)$-polarization mode.

case of x=0.35, F_2 and F_3 are almost degenerate along the *M*-*R* direction, while $F_1(F_3)$ and $F_2(F_4)$ are along the *R*-*X* direction. It is in good agreement with the ARPES-measured ones as shown in Figs. 4(c)–4(f). Among these four bands, only three (blue curves) cross at *R*, forming a sixfold DP or a sextuple point. The band calculation predicts that there is another sextuple point in the valence band part, as drawn with the three green curves. The energy gap between the two sixfold degenerate DPs is predicted to be ∼0.02 eV, but the ARPES-measured gap is ∼5 times larger than the prediction. The calculated gap size can be tuned to the experimental value by introducing a small variation in the crystal structure. When we increase the Sb position parameter x to 0.38, it becomes comparable to the experimental ones as shown in Figs. 4(b) and 4(c). However, the band dispersions deviate from the experiments instead. In this case, the four bands, F_1–F_4, in the *M*-*R* direction are calculated to almost overlap one another, but the ARPES data in Fig. 4(d) clearly shows the split band dispersions as in Fig. 4(a). This behavior is interpreted as a result of the competition between the band energies and the crystal symmetries that protect the sixfold DPs. Considering the fact that our previous XRD pattern analysis determined the parameter to be 0.3745, the sensitivity of the FLF structure on the Sb position parameter could be beyond the accuracy of GGA calculation method.

Sixfold degeneracy of the DP can be explicitly confirmed in our ARPES data. Since the system has two mirror planes orthogonal to each other, it has two equivalent orthogonal high symmetric lines for each *R*-*M* and *R*-*X*, respectively. To distinguish them, we denote *R*-*M'* and *R*-*X'* in Figs. 4(d) and 4(f). Their momentum directions are drawn with red dotted lines in the ARPES-measured FS as shown in Fig. 4(g). The evolution of the FLF with an increasing binding energy is presented in Figs. 4(g)–4(k). The measured FLF does not look so symmetric as theory predicts, but it is quite often observed in ARPES because the photoemission intensity is determined by a matrix element effect, which is a function of the photon energy, the photon polarization vector, and the initial/final states of the photoelectrons [25]. These features can also be clearly seen in the ARPES-measured FLFs in Fig. 2. Sometimes, they can be even utilized to resolve almost degenerate states with different characters as is in this case. In the *M*-*R*-*M* direction data of Fig. 4(c), only F_1 is resolved from the others, but F_4 is also resolved in *M'*-*R*-*M'* direction data of Fig. 4(d). The similar resolving happens in the *X*-*R*-*X* and *X'*-*R*-*X'* directions. Only $F_{3,4}$ are seen in the *X*-*R*-*X* direction data of Fig. 4(e), while only $F_{1,2}$ are in the *X'*-*R*-*X'* direction data of Fig. 4(f). Since each $F_{1,2,3,4}$ is a doubly degenerate state, our ARPES data confirm the sixfold degeneracy of the DP in the FLF.

To experimentally confirm the orbital characters of the FLF, we performed polarization-dependent ARPES measurements as summarized in Figs. 5(a)–5(e). Our experimental setup is depicted in Fig. 5(a). The lattice vector $\vec{a}$ of the sample was rotated around the sample normal by 45° from the horizontal axis. Under the experimental geometry, we obtained ARPES data for the FLF with $p(s)$-polarization mode as shown in the upper (lower) panels of Fig. 5. The middle panels show a constant energy map of the calculated FLF structure at each energy. A prominent difference between the p-polarization and s-polarization data appears in the inner parts of the FLF. In the s-polarization data, the inner states of the FLF are observed while they are almost absent in the p-polarization data. This is more clearly seen in the dispersion images of Fig. 5(e). The difference can be explained by taking the orbital characters of the FLF into account. Photoemission intensity is proportional to the square of the matrix element $M_{fi} = \langle f|\vec{A}\cdot\vec{p}|i\rangle$, where $\langle f|$, $|i\rangle$, $\vec{A}$, and $\vec{p}$ are the final state bra-vector, the initial state ket-vector, the vector potential of the photon, and the momentum operator of the electron. Under our experimental geometry, the parity of the final state with respect to the mirror plane is always $+1$, and the parity of $\vec{A}\cdot\vec{p}$ is $+1(-1)$ for $p(s)$ polarization. The main orbital characters of the FLF are Pd $4d_{x^2-y^2/3z^2-r^2}$'s from four different sites. This is easily understandable if we consider the fact that Pd ions are located at the center of an Sb octahedron, so they feel an O_h-type crystal electric field that splits five degenerate d orbitals into triply degenerate t_{2g} states at a lower energy and doubly degenerate e_g states at a higher energy. Since each Pd ion has nine electrons in the $4d$'s, the FLF near the Fermi level consists of Pd $4d_{e_g}$'s, i.e., $4d_{x^2-y^2/3z^2-r^2}$'s. It is noteworthy that the parity of $d_{x^2-y^2}(d_{3z^2-r^2})$ with respect to the mirror plane is $-1(+1)$. In the p-polarization mode, the matrix element is $M_{fi} = \langle +|+|-\rangle = 0$ for $|i\rangle = |d_{x^2-y^2}\rangle$, and $M_{fi} = \langle +|+|+\rangle \neq 0$ for $|i\rangle = |d_{3z^2-r^2}\rangle$. Thus, only $d_{3z^2-r^2}$ character is observed. Similarly, the s-polarization mode detects only $d_{x^2-y^2}$ character. Applying this parity argument to our data, the main orbital character of the inner square part of the FLF is Pd $4d_{x^2-y^2}$ but the outer part has a mixed character of $4d_{x^2-y^2}$ and $4d_{3z^2-r^2}$.

IV. CONCLUSION

We report detailed angle-resolved photoemission measurements on the electronic structure of an unconventional multifold Dirac fermionic semimetal $PdSb_2$ with a pyrite structure. By exploiting the photon energy and polarization dependence of the matrix element in photoemission intensity and by comparing the photoemission data with *ab initio* band calculations, we can experimentally identify the exact structure including the orbital characters of the electron pockets at the R point in the BZ of $PdSb_2$. Each electron pocket and hole-pocket-like structure consists of three doubly degenerate parabolic bands, respectively, which cross one another at the R point, forming a sixfold Dirac fermion. The overall electronic structure is consistent with the band-calculation results, but the gap size between two sextuple points is very sensitive to the Wyckoff position of Sb atoms, which implies the competitive relation between the band energies and the crystal symmetries.

ACKNOWLEDGMENTS

This work was supported by the National Research Foundation (NRF) of Korea Grant funded by the Korean Government (MEST) (Grant No. 2019R1I1A3A0105818813). The theoretical calculations were supported in part by KAERI Internal R&D Program (No. 524460-22) and by the National Superconducting center KISTI (No. KSC-2020-CRE-0251).

[1] M. Z. Hasan and C. L. Kane, Rev. Mod. Phys. **82**, 3045 (2010).
[2] X.-L. Qi and S.-C. Zhang, Rev. Mod. Phys. **83**, 1057 (2011).
[3] K. Park, J. Korean Phys. Soc. **73**, 817 (2018).
[4] C. L. Kane and E. J. Mele, Phys. Rev. Lett. **95**, 146802 (2005).
[5] H.-J. Noh, H. Koh, S.-J. Oh, J.-H. Park, H.-D. Kim, J. D. Rameau, T. Valla, T. E. Kidd, P. D. Johnson, Y. Hu, and Q. Li, Europhys. Lett. **81**, 57006 (2008).
[6] D. Hsieh, D. Qian, L. Wray, Y. Xia, Y. S. Hor, R. J. Cava, and M. Z. Hasan, Nature **452**, 970 (2008).
[7] S. Murakami, New J. Phys. **9**, 356 (2007).
[8] X. Wan, A. M. Turner, A. Vishwanath, and S. Y. Savrasov, Phys. Rev. B **83**, 205101 (2011).
[9] Z. K. Liu, B. Zhou, Y. Zhang, Z. J. Wang, H. M. Weng, D. Prabhakaran, S.-K. Mo, Z. X. Shen, Z. Fang, X. Dai, Z. Hussain, AND Y. L. Chen, Science **343**, 864 (2014).
[10] S. M. Young, S. Zaheer, J. C. Y. Teo, C. L. Kane, and E. J. Mele, and A. M. Rappe, Phys. Rev. Lett. **108**, 140405 (2012).
[11] A. H. Castro Neto, F. Guinea, N. M. R. Peres, K. S. Novoselov, and A. K. Geim, Rev. Mod. Phys. **81**, 109-162 (2009).
[12] B. Q. Lv, H. M. Weng, B. B. Fu, X. P. Wang, H. Miao, J. Ma, P. Richard, X. C. Huang, L. X. Zhao, G. F. Chen, Z. Fang, X. Dai, T. Qian, and H. Ding, Phys. Rev. X **5**, 031013 (2015).
[13] A. A. Soluyanov, D. Gresch, Z. Wang, Q. Wu, M. Troyer, X. Dai, and B. A. Bernevig, Nature **527**, 495 (2015).
[14] H. Huang, S. Zhou, and W. Duan, Phys. Rev. B **94**, 121117(R) (2016).
[15] H.-J. Noh, J. Jeong, E.-J. Cho, K. Kim, B. I. Min, and B.-G. Park, Phys. Rev. Lett. **119**, 016401 (2017).
[16] B. Bradlyn, J. Cano, Z. Wang, M. G. Vergniory, C. Felser, R. J. Cava, and B. A. Bernevig, Science **353**, aaf5037 (2016).
[17] B. Q. Lv, Z.-L. Feng, Q.-N. Xu, X. Gao, J.-Z. Ma, L.-Y. Kong, P. Richard, Y.-B. Huang, V. N. Strocov, C. Fang, H.-M. Weng, Y.-G. Shi, T. Qian, and H. Ding, Nature **546**, 627 (2017).
[18] Z. Rao, H. Li, T. Zhang, S. Tian, C. Li, B. Fu, C. Tang, L. Wang, Z. Li, W. Fan, J. Li, Y. Huang, Z. Liu, Y. Long, C. Fang, H. Weng, Y. Shi, H. Lei, Y. Sun, T. Qian, and H. Ding, Nature **567**, 496 (2019).
[19] N. B. Schröter, D. Pei, M. G. Vergniory, Y. Sun, K. Manna, F. de Juan, J. A. Krieger, V. Süss, M. Schmidt, P. Dudin, B. Bradlyn, T. K. Kim, T. Schmitt, C. Casho, C. Felser, V. N. Strocov, and Y. Chen, Nat. Phys. **15**, 759 (2019).
[20] N. Kumar, M. Yao, J. Nayak, M. G. Vergniory, J. Bannies, Z. Wang, N. B. M. Schröter, V. N. Strocov, L. Müchler, W. Shi, E. D. L. Rienks, J. L. Mañes, C. Shekhar, S. S. P. Parkin,

J. Fink, G. H. Fecher, Y. sun, B. A. Bernevig, and C. Felser, Adv. Mater. **32**, 1906046 (2020).
[21] Z. P. Sun, C. Q. Hua, X. L. Liu, Z. T. Liu, M. Ye, S. Qiao, Z. H. Liu, J. S. Liu, Y. F. Guo, Y. H. Lu, and D. W. Shen, Phys. Rev. B **101**, 155114 (2020).
[22] X. Yáng, T. A. Cochran, R. Chapai, D. Tristant, J.-X. Yin, I. Belopolski, Z. Chéng, D. Multer, S. S. Zhang, N. Shumiya, M. Litskevich, Y. Jiang, G. Chang, Q. Zhang, I. Vekhter, W. A. Shelton, R. Jin, S.-Y. Xu, and M. Z. Hasan, Phys. Rev. B **101**, 201105(R) (2020).
[23] R. Chapai, Y. Jia, W. A. Shelton, R. Nepal, M. Saghayezhian, J. F. DiTusa, E. W. Plummer, C. Jin, and R. Jin, Phys. Rev. B **99**, 161110(R) (2019).
[24] H.-D. Kim, C.-H. Min, B. J. Kim, D.-Y. Cho, S.-J. Oh, J.-Y. Kim, J. H. Kim, and T.-H. Kang, AIP Conf. Proc. **879**, 477 (2007).
[25] A. Damascelli, Phys. Scr. **T109**, 61 (2004).
[26] K. Koepernik and H. Eschrig, Phys. Rev. B **59**, 1743 (1999).
[27] M. C. Neale, M. D. Hunter, J. N. Pritikin, M. Zahery, T. R. Brick, R. M. Kirkpatrick, R. Estabrook, T. C. Bates, H. H. Maes, and S. M. Boker, OpenMX 2.0: Extended structural equation and statistical modeling, Psychometrika **81**, 535 (2016).
[28] T. Roisnel and J. Rodriguez-Carvajal, FullProf 2000.
[29] Th. Hahn, *International Tables for Crystallography*, 5th ed. (Springer, The Netherlands, 2005).
[30] S. Furuseth, A. Selte, and A. Kjekshus, Acta Chem. Scand. **19**, 735 (1965).
[31] V. N. Strocov, J. Electron Spectrosc. Relat. Phenom. **130**, 65 (2003).
[32] See Supplemental Material at http://link.aps.org/supplemental/10.1103/PhysRevB.106.205125 for further information on the surface band structure. Also see Refs. [33–35] for calculation details.
[33] N. E. Brese and H. G. von Schnering, Z. Anorg. Allg. Chem. **620**, 393 (1994).
[34] M. P. López-Sancho, J. M. López-Sancho, and J. Rubio, J. Phys. F: Met. Phys. **14**, 1205 (1984).
[35] M. P. López-Sancho, J. M. López-Sancho, and J. Rubio, J. Phys. F: Met. Phys. **15**, 851 (1985).